lubricants

MDPI

Article

A Physics–Data Hybrid Framework for Friction Interface Temperature-Field Prediction Based on Experimentally Corrected Finite Element Analysis

Jianpeng Wu [1,2,*], Xingyuan Jia [1,2], Nikolaos Rogkas [3,4], Ao Ding [1,2] and Xinchao Lin [1,2]

[1] School of Mechanical Engineering, Beijing Information Science & Technology University, Beijing 100192, China; 18840177305@163.com (X.J.); aoding-odin@outlook.com (A.D.); 13067119925@163.com (X.L.)
[2] Key Laboratory of Modern Measurement and Control Technology, Ministry of Education, Beijing Information Science & Technology University, Beijing 100192, China
[3] Chemical Process & Energy Resource Institute, Centre for Research & Technology Hellas, Aigialias 52, 15125 Marousi, Greece; n.rogkas@certh.gr
[4] Machine Design Laboratory, National Technical University of Athens, NTUA Zografou Campus, 15780 Athens, Greece
* Correspondence: 15811319103@163.com

Abstract

Accurate characterization of the friction interface temperature field is essential for assessing thermal conditions and ensuring the reliable operation of wet friction components. However, direct acquisition of the complete transient temperature field remains difficult under multiple operating conditions. To address this limitation, a physics–data hybrid framework based on experimentally corrected finite element data is proposed. Experimental temperature measurements are used to validate and spatially correct the finite element method (FEM)-based temperature field, yielding an experimentally constrained complete-field dataset. The proper orthogonal decomposition (POD) method extracts the dominant spatial modes, while the radial basis function (RBF) model maps pressure, rotational speed, and sliding duration to the modal coefficients, enabling rapid reconstruction under unseen operating conditions. The POD-RBF model achieves a coefficient of determination (R^2) of 0.956, with a mean absolute error (MAE) of 3.301 °C and a root mean square error (RMSE) of 7.380 °C. Sensitivity analysis indicates that prediction accuracy is most sensitive to the RBF shape parameter, followed by the smoothing parameter and the number of retained POD modes; among the operating-condition parameters, sliding duration has the greatest influence. Further analysis shows that increasing pressure and rotational speed intensifies both the temperature rise and spatial temperature nonuniformity at the friction interface. The proposed framework provides an effective approach for rapid prediction of complete temperature fields under multiple operating conditions.

Keywords: wet friction component; temperature field prediction; finite element correction; proper orthogonal decomposition; radial basis function

Check for updates

Received: 6 October 2026
Revised: 12 November 2026
Accepted: 14 November 2026
Published: 18 November 2026

Copyright: © 2026 by the authors. Licensee MDPI, Basel, Switzerland. This article is an open access article distributed under the terms and conditions of the Creative Commons Attribution (CC BY) license.

1. Introduction

Wet friction components are widely used in automatic transmissions, construction machinery, and marine transmission systems, where power transmission and operating-condition switching are achieved through the engagement and disengagement of friction pairs. During engagement, relative sliding between the friction disc and the mating disc

rapidly converts mechanical energy into frictional heat, resulting in a significant and nonuniform temperature rise at the interface. Local heat accumulation may cause changes in lubrication performance, hot spots, and thermal deformation, thereby affecting the operating stability and service life of the friction components. Furthermore, under the combined effects of pressure, rotational speed, and sliding duration, the interface temperature exhibits strong temporal variation and spatial nonuniformity. Local temperature measurements alone are therefore insufficient to fully characterize the temperature rise and distribution. Accurate acquisition of the complete transient temperature field under different operating conditions is essential for analyzing the thermal characteristics of wet friction interfaces.

The temperature field of wet friction interfaces is extensively investigated through theoretical, numerical, and experimental approaches. Zagrodzki [1] and Jen et al. [2] investigate the transient temperature field and temperature rise of wet clutches during a single engagement, and the validity of the numerical models is verified experimentally. The finite element method (FEM) is employed by Li et al. [3,4] to analyze transient temperature fields and radial and circumferential temperature differences. The effects of rotational speed, pressure, friction coefficient, and cooling conditions on temperature distributions are further investigated by Lin et al. [5] and Wu et al. [6]. Real-time temperature calculation and prediction for wet multi-disc clutches are studied by Groetsch et al. [7], while the temperature field description is improved by Jin et al. [8] from the perspective of energy flow at the sliding interface. Complementary experimental work for dip-lubricated wet clutches has quantified frictional work during engagement from torque and relative-speed responses, showing that its dependence on lubricant fill volume varies with initial rotational speed [9]. These studies provide an important basis for analyzing the temperature rise of wet friction interfaces. However, numerical results remain affected by uncertainties in material properties, contact conditions, and heat transfer boundaries. In addition, only a limited number of temperature measurement points can generally be obtained experimentally because of the structural constraints and rotational motion of the friction pair, making direct acquisition of the complete temperature field difficult.

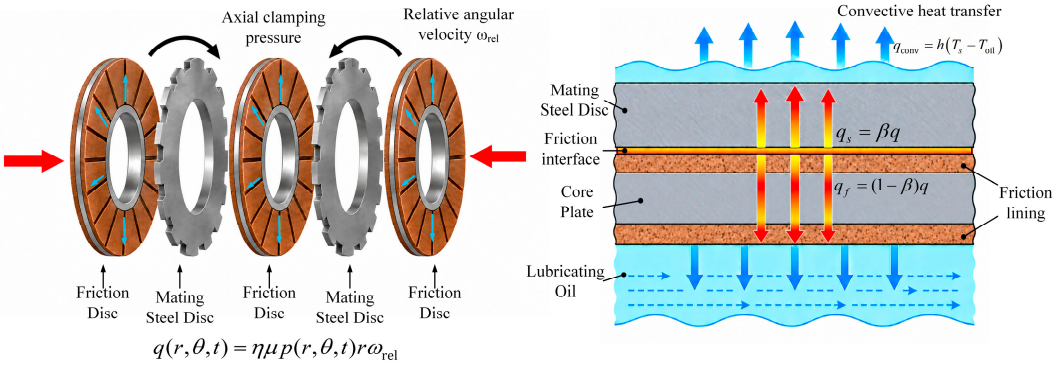
The integration of numerical simulation, measurement data, and reduced-order modeling provides an alternative approach to complete temperature-field reconstruction. Gappy proper orthogonal decomposition is combined with local temperature measurements by Lei et al. [10] to reconstruct the complete temperature field. Jiang et al. [11] and Wang et al. [12] further demonstrate that high-dimensional temperature fields can be effectively recovered by combining proper orthogonal decomposition (POD) with sparse measurement data. The combination of POD and surrogate models allows high-dimensional nodal temperature prediction to be transformed into low-dimensional modal coefficient prediction. POD and a radial basis function (RBF) model are combined by Peng et al. [13] for rapid temperature-field prediction in complex thermal processes. Reduced-order features and a surrogate model are used by Liu et al. [14] for rapid solution of three-dimensional temperature fields, while the time variable is introduced into the POD-RBF parameter space by Zhao et al. [15] to predict transient temperature fields. Furthermore, data-driven models have so far been directed mainly at the open-clutch state, where for instance Gaussian process regression trained on experiments has been used to map groove design and operating parameters to drag losses [16]. However, limited attention has been given to integrating experimental measurements, corrected finite-element models, and reduced-order prediction for wet clutch temperature fields under multiple operating conditions. The importance of such an approach is given by the fact that design and control of wet clutches increasingly rely on optimization and real-time estimation, both of which require fast temperature field calculations across the whole operating range, but without sacrificing the accuracy that only experimentally validated models can provide.

Therefore, to address this gap, this study proposes a coupled FEM-POD-RBF method for friction interface temperature-field prediction. The finite element temperature field is validated and corrected using experimental temperature measurements, and a complete-field dataset constrained by experimental data is constructed. The dominant spatial modes are extracted using POD, and the mapping between operating-condition parameters and modal coefficients is established using RBF to enable rapid reconstruction of the complete temperature field under unseen operating conditions. Prediction performance is evaluated using representative test conditions, model comparison, and sensitivity analysis, while the effects of pressure and rotational speed on the temperature rise and temperature distribution characteristics of the friction interface are also analyzed.

2. Mechanism

2.1. Frictional Heat Generation and Heat Transfer

During the sliding process of wet friction components, the operating-condition parameters affect the frictional heat input and heat transfer at the interface, resulting in a transient and nonuniform temperature field [17,18]. Accordingly, frictional heat generation, heat flux partition, heat conduction within the materials, and boundary heat transfer are considered in the finite-element model. The frictional heat generation and heat transfer mechanisms of the wet friction pair are illustrated in Figure 1. Figure 1a illustrates the engagement process of the friction pair, and Figure 1b illustrates the mechanisms of frictional heat generation and heat transfer.



(**a**) Frictional heat generation (**b**) Heat transfer and heat flux partition

Figure 1. Thermal heat generation and heat transfer mechanisms of the wet friction pair.

During engagement, relative sliding occurs between the friction disc and the mating steel disc under normal pressure, converting mechanical energy into frictional heat. The local frictional heat flux at a position (r,θ) on the friction interface can be expressed as:

$$q(r,\theta,t) = \eta\mu p(r,\theta,t) r\omega_{\mathrm{rel}} \tag{1}$$

where q is the local frictional heat flux, η is the fraction of frictional work converted into heat, μ is the friction coefficient, p is the local contact pressure, r is the radial position, θ is the circumferential coordinate, and ω_{rel} is the relative angular velocity between the friction disc and the mating steel disc.

Because the friction disc and the mating steel disc have different thermophysical properties, the generated frictional heat is partitioned between the two components. The heat partition coefficient for the mating steel disc is defined as

$$\beta = \frac{\sqrt{\lambda_s \rho_s c_s}}{\sqrt{\lambda_s \rho_s c_s} + \sqrt{\lambda_f \rho_f c_f}} \tag{2}$$

where β is the heat partition coefficient for the mating steel disc; λ_s, ρ_s, and c_s are the thermal conductivity, density, and specific heat capacity of the mating steel disc, respectively; λ_f, ρ_f, and c_f are the corresponding properties of the friction disc. The terms $\sqrt{\lambda_s \rho_s c_s}$ and $\sqrt{\lambda_f \rho_f c_f}$ represent the thermal effusivities of the mating steel disc and friction disc, respectively.

The frictional heat generated at the interface is partitioned according to the thermophysical properties of the two materials. The heat flux entering the mating steel disc is expressed as

$$q_s = \beta q \tag{3}$$

After entering the two components, the frictional heat is transferred into the material by heat conduction. The transient temperature field satisfies the three-dimensional heat conduction equation:

$$\rho c \frac{\partial T}{\partial t} = \lambda \left(\frac{\partial^2 T}{\partial x^2} + \frac{\partial^2 T}{\partial y^2} + \frac{\partial^2 T}{\partial z^2} \right) \tag{4}$$

where ρ is the material density, c is the specific heat capacity, t is time, and x, y, and z are the spatial coordinates.

In addition to heat conduction within the friction pair, convective heat transfer occurs between the wet friction components and the lubricating oil. When the component surface temperature is higher than the oil temperature, the convective heat flux is expressed according to Newton's law of cooling as

$$q_{\text{conv}} = h(T_s - T_{\text{oil}}) \tag{5}$$

where q_{conv} is the convective heat flux, h is the convective heat transfer coefficient, T_s is the surface temperature of the friction component, and T_{oil} is the lubricating oil temperature. Lubricating oil flow and distribution around rotating transmission components depend strongly on oil temperature, rotational speed, surface characteristics, and oil supply conditions [19,20].

In the finite-element model, the frictional heat flux and heat partition are determined according to the actual geometry and material properties of the friction pair. The transient heat conduction equation is solved in Abaqus with the corresponding thermal boundary conditions to obtain the complete friction interface temperature field under different pressures, rotational speeds, and sliding durations.

2.2. Finite-Element Model

A finite-element model of the friction disc and mating steel disc is established in Abaqus. The actual geometry is simplified according to the structural characteristics of the friction pair, and a hexahedral mesh is generated using C3D8RT elements. A mesh independence analysis is performed to determine an appropriate mesh density for the temperature field simulation. Several mesh configurations are evaluated based on the predicted maximum interface temperature. The results showed that the predicted maximum interface temperature changed negligibly as the mesh density increased. Therefore, the selected mesh is considered sufficient to maintain numerical accuracy while limiting computational cost. The finite-element model and mesh of the friction disc and mating steel disc are shown in Figure 2. The friction disc is defined as the active component and the mating steel disc as the driven component, while the sliding process is simulated using surface-to-surface contact.

The mating steel disc is made of 65Mn steel, whereas the friction disc is made of a copper-based powder metallurgy friction material. The corresponding geometric and material parameters are listed in Table 1.

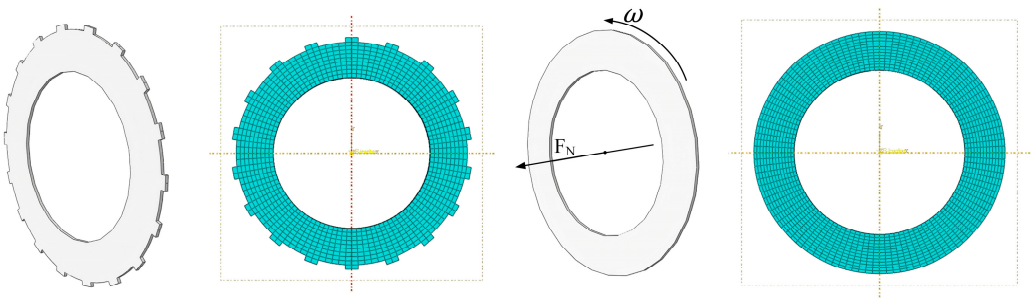


Figure 2. Finite-element model and mesh of the wet friction pair.

Table 1. Geometric and physical parameters of the friction pair.

Parameter	Friction Disc	Mating Steel Disc
Density ρ/(kg·m^{-3})	5600	7800
Thickness/mm	2	3
Outer diameter/mm	125	125
Inner diameter/mm	85	85
Thermal expansion coefficient α	1.30×10^{-5}	1.27×10^{-5}
Elastic modulus E/GPa	110	160
Thermal conductivity λ /(W·m^{-1}·°C^{-1})	30	See Table 2
Specific heat capacity c /(J·kg^{-1}·°C $^{-1}$)	536	487
Poisson's ratio ν	0.30	0.29

Table 2. Thermal conductivity of the mating steel disc.

Temperature/°C	Thermal Conductivity λ/(W·m^{-1}·°C $^{-1}$)
20	51.2
100	50.9
200	50.3
300	46.8
400	43.5

The normal load is applied using a smooth-step amplitude, increasing from zero to the prescribed level during the initial 0.01 s and remaining constant thereafter. The friction coefficient is calculated using an empirical relationship established for Cu-based wet clutch friction pairs, as expressed in Equation (6) [21].

$$\mu = 23\mathrm{e}^{\left[\frac{-2.6v}{(\ln T-3.2)((28.3p)^{0.4}-0.87)}-5.16\right]} + \frac{0.01\ln(4v+1)}{\mathrm{e}^{0.005T}} + 0.08(\mathrm{e}^{-0.005T}-1)(\mathrm{e}^{-0.2v}-1) - 0.005\ln(28.3p) + 0.035 \quad (6)$$

where μ is the friction coefficient, v is the relative sliding velocity, p is the average contact pressure, and T is the friction surface temperature. The friction coefficient is calculated using the corresponding operating parameters for each condition and assigned to the tangential contact property.

The thermal conductivity of the mating steel disc decreases with increasing temperature. Therefore, the temperature-dependent thermal conductivity values listed in Table 2 are used.

Thermal boundary conditions mainly account for heat conduction within the friction pair and convective heat transfer with the cooling oil. Thermal radiation and heat exchange with the surrounding air are neglected because of their limited effects during the short sliding period. The convective heat transfer coefficient of wet friction components is influenced

by rotational speed, lubricant flow conditions, oil temperature, and surface characteristics. However, comparisons under a representative short-duration sliding condition showed that the variation in the considered heat transfer coefficient was relatively limited and had only a minor influence on the overall temperature distribution. Therefore, constant convective heat transfer coefficients of 1300 W/(m^2·K) and 100 W/(m^2·K) are adopted for the friction surfaces and the inner and outer circumferential surfaces, respectively.

For the motion constraints, all translational and rotational degrees of freedom of the mating steel disc are constrained to maintain a fixed state during sliding. For the friction disc, the translational degrees of freedom and rotational degrees of freedom perpendicular to the rotation axis are constrained, while only the rotational degree of freedom about the central axis is released to enable relative sliding under the applied normal load.

3. Experiment

3.1. Test Equipment and Procedure

The experiments are conducted on a wet friction component test bench, as shown in Figure 3. The experimental components include a friction disc and a mating steel disc, whose geometric dimensions and material properties are consistent with those used in the finite-element model. The finite-element model is established based on this friction pair. To obtain the transient temperature responses at different spatial locations of the friction interface, 12 K-type thermocouples (measurement range: 0–800 °C) are embedded in the mating steel disc near the friction surface. The sensing junctions were positioned approximately 1 mm below the friction contact surface. The thermocouples comply with the Class 2 tolerance requirements specified in IEC 60584-1, with a permissible error of ±2.5 °C or ±0.75% of the measured temperature, whichever is greater. The thermocouple response time is 0.1–0.3 s. Temperature data are acquired at a sampling frequency of 100 Hz, corresponding to a sampling interval of 0.01 s. The measurement points are uniformly distributed in the circumferential direction at intervals of 30° and are arranged alternately at the inner, middle, and outer radii. Four measurement points are placed at each radial position, with a circumferential spacing of 90° between adjacent points at the same radius. Each measurement point is matched with the corresponding spatial location in the finite-element model to allow comparison between the experimental measurements and the finite element results.

An orthogonal experimental design was adopted to investigate the effects of different operating parameters on the temperature response of the wet friction components. Three factors were considered: rotational speed, pressure, and sliding duration. The rotational speed ranged from 400 to 2000 r/min, the test pressure ranged from 0.6 to 3.0 MPa, and three sliding-duration levels of 0.5, 1.0, and 1.5 s were considered. The experimental conditions were established by combining different levels of these three factors. Before each test, the friction components were restored to the specified initial temperature and stabilized at the target rotational speed. The prescribed pressure was then applied, and the instant when the friction disc reached the target rotational speed and stable relative sliding was achieved was defined as zero time. The temperatures at all measurement points were recorded simultaneously. Each operating condition was tested three times to assess the repeatability of the experimental measurements.

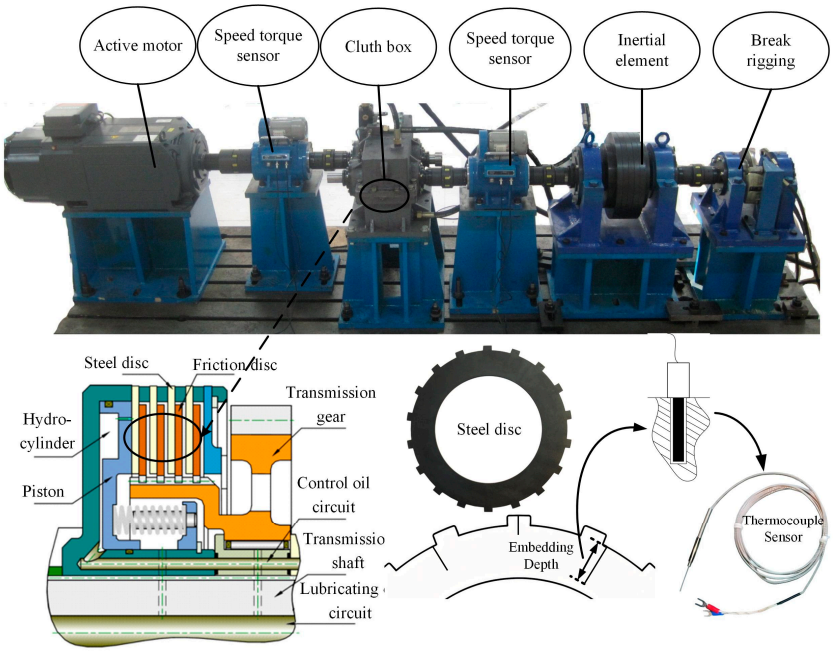


Figure 3. Wet friction component test bench and thermocouple measurement system.

3.2. Finite-Element Model Correction

To evaluate the capability of the finite-element model to characterize the transient temperature variation and spatial temperature distribution of the wet friction interface, the thermocouple measurement points are matched with the corresponding nodes in the finite-element model under identical pressure, rotational speed, sliding duration, and initial temperature conditions. Three representative measurement points, P1, P2, and P3, located at the inner, middle, and outer radial positions of the friction interface, respectively, are selected to compare the measured temperature histories with the calculated temperatures at the corresponding finite element nodes. As shown in Figure 4, the temperature variation trends predicted by the finite-element model agree well with the experimental measurements at the three representative points.

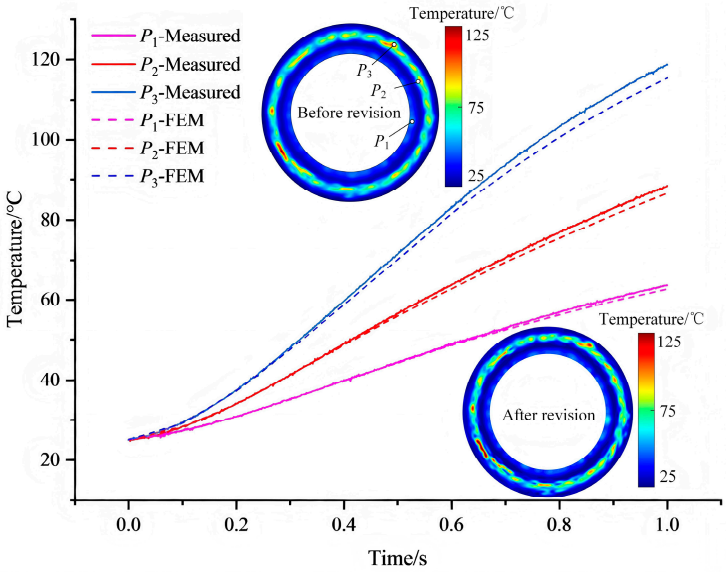


Figure 4. Comparison of measured and finite element temperature at representative measurement points.

To quantify the accuracy of the finite-element model before experimental correction, the mean absolute error (MAE), root mean square error (RMSE), and mean relative error (MRE) were calculated by comparing the simulated temperatures with the corresponding experimental measurements under five representative operating conditions. The results are summarized in Table 3.

Table 3. Validation results of the finite-element model under different operating conditions.

Pressure/MPa	Rotational Speed/(r/min)	MAE/°C	RMSE/°C	MRE/%
1.5	1500	3.824	4.967	4.21
1.5	1000	3.157	4.086	3.58
1	1500	2.743	3.638	3.21
1.5	500	2.216	2.984	2.74
2	1500	4.368	5.617	4.76

The MAE, RMSE, and MRE values between the finite element results and experimental measurements range from 2.216 to 4.368 °C, 2.984 to 5.617 °C, and 2.74% to 4.76%, respectively. The average MAE, RMSE, and MRE are 3.262 °C, 4.258 °C, and 3.70%, respectively. The relatively low error levels under different operating conditions demonstrate that the finite-element model can effectively capture the overall temperature rise and the principal temperature variation characteristics of the wet friction interface. However, the prediction errors vary under different pressures and rotational speeds, indicating that uncertainties associated with material properties, contact conditions, and thermal boundary conditions may exist during wet friction operation. These uncertainties are difficult to completely eliminate in the finite-element model due to the simplification of actual contact behavior, material variability, and complex heat transfer conditions. The experimental temperature measurements are therefore introduced to further correct the temperature field while retaining the complete spatial information provided by the finite-element model.

The finite element results are corrected using the experimental temperature measurements while the complete spatial distribution of the finite element temperature field is retained. The temperature residual at the ith measurement point at time t is defined as

$$\Delta T_i(t) = T_{\mathrm{exp},i}(t) - T_{\mathrm{FEM},i}(t) \tag{7}$$

where $T_{\mathrm{exp},i}(t)$ is the measured temperature at the ith measurement point, $T_{\mathrm{FEM},i}(t)$ is the finite element temperature at the corresponding location, and $\Delta T_i(t)$ is the temperature residual between them.

Because the experimental measurements provide temperature information only at a limited number of spatial locations, whereas the finite-element model provides a continuous temperature distribution over the entire friction interface, the discrete measurement residuals are extended to the complete interface. The spatial continuity of the temperature deviation is considered, and the residuals are weighted according to the distance between each finite element node to be corrected and the measurement points. For an arbitrary location (x,y) on the friction interface, the distance to the ith measurement point is expressed as

$$d_i(x,y) = \sqrt{(x - x_i)^2 + (y - y_i)^2} \tag{8}$$

where (x_i,y_i) denotes the spatial coordinates of the ith thermocouple measurement point, and (x,y) denotes the coordinates of the finite element node to be corrected.

$$w_i(x,y) = \frac{1}{[d_i(x,y) + \delta]^k} \tag{9}$$

where $w_i(x,y)$ is the weight of the ith measurement point for the node to be corrected, k is the distance-weighting exponent, and δ is a small positive constant introduced to avoid a

zero denominator at the measurement point. A measurement point closer to the target node is assigned a larger weight, and its temperature residual therefore contributes more strongly to the local correction. The distance-weighting exponent k and the regularization parameter δ are selected using a predefined grid search. Candidate parameter combinations are evaluated based on the RMSE between the corrected and measured temperature histories. The combination yielding the lowest cross-validated RMSE is selected for the subsequent temperature-field correction.

Based on the temperature residuals and the spatial weights, the temperature correction at an arbitrary location on the friction interface is expressed as

$$\Delta T(x,y,t) = \frac{\sum_{i=1}^{12} w_i(x,y)\Delta T_i(t)}{\sum_{i=1}^{12} w_i(x,y)} \tag{10}$$

The spatial residual field is superimposed on the original finite element temperature field node by node, yielding the experimentally corrected complete temperature field:

$$T_{\mathrm{cor}}(x,y,t) = T_{\mathrm{FEM}}(x,y,t) + \Delta T(x,y,t) \tag{11}$$

where $T_{\mathrm{cor}}(x,y,t)$ is the corrected temperature, $T_{\mathrm{FEM}}(x,y,t)$ is the original finite element temperature, and $\Delta T(x,y,t)$ is the spatial correction obtained from the measured temperature residuals.

The accuracy of the corrected temperature field at locations not used for correction is evaluated using leave-one-out cross-validation based on the 12 thermocouple measurement points. In each fold, one point is withheld, while the remaining eleven points are used for parameter selection and temperature-field correction. The predicted temperature at the withheld point is compared with the corresponding experimental measurement. After correction, the MAE decreases from 3.487 °C to 1.826 °C, representing a reduction of 47.63%, while the RMSE decreases from 4.613 °C to 2.374 °C, representing a reduction of 48.54%. These results indicate that the proposed correction method improves the temperature prediction accuracy at the withheld measurement locations.

By weighting the measurement residuals according to spatial distance and superimposing them on the original finite element temperature field, experimental temperature information is incorporated while the spatial distribution characteristics of the finite-element model are retained. The resulting corrected temperature field is used for subsequent temperature-field prediction.

4. Temperature-Field Prediction

4.1. FEM-POD-RBF Temperature-Field Prediction Framework

To achieve rapid prediction of the complete friction interface temperature field under different operating conditions, an FEM-POD-RBF temperature-field prediction framework is developed, as shown in Figure 5. The framework integrates finite element simulation, experimental temperature correction, POD-based dimensionality reduction, and RBF-based nonlinear mapping to establish the relationship between operating conditions and complete temperature fields.

A total of 873 operating-condition samples are used in this study and divided into a training set, a validation set, and an independent test set, comprising 613, 130, and 130 samples, respectively. During model development, the 613 training samples are used to estimate the input normalization parameters, construct the POD basis, estimate the normalization parameters for the modal coefficients, and fit the RBF model. The 130 validation samples are used for model selection, hyperparameter tuning, and model-parameter sensitivity analysis. After the final model configuration is determined, the training and validation sets are

combined, and the relevant preprocessing parameters and POD basis are re-estimated using all 743 development samples before the final RBF model is refitted. The independent test set is reserved exclusively for final model performance evaluation to assess the predictive capability of the model under operating conditions that are not used during development.

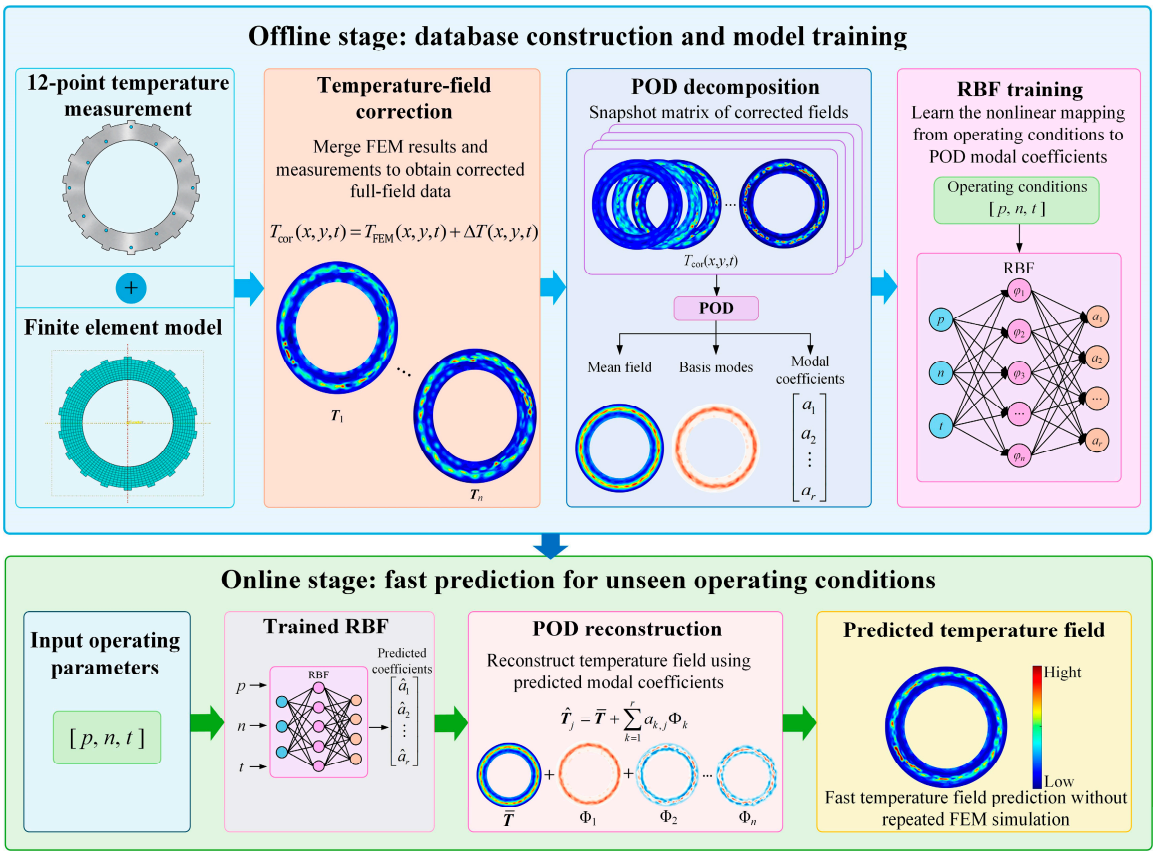


Figure 5. Framework of the FEM-POD-RBF temperature-field prediction method.The finite element temperature fields are first corrected using experimental temperature measurements to construct an experimentally constrained temperature field database. POD is then applied to extract the dominant spatial modes of the corrected temperature fields, transforming the high-dimensional temperature field into low-dimensional modal coefficients. An RBF model is trained to establish the nonlinear relationship between operating conditions (pressure, rotational speed, and sliding duration) and the POD modal coefficients. For unseen operating conditions, the trained RBF model predicts the corresponding modal coefficients, and the complete temperature field is reconstructed by combining the predicted coefficients with the retained POD modes. Therefore, the proposed framework enables rapid prediction of complete temperature fields without repeated finite element simulations while preserving the spatial characteristics of the friction interface.

In this framework, high-dimensional nodal temperature prediction is transformed into low-dimensional modal coefficient prediction, thereby reducing the computational complexity of temperature-field prediction. The main parameter settings of the POD-RBF model used in the subsequent analyses are summarized in Table 4.

Table 4. Main parameters of the POD-RBF model.

Hyperparameter	Setting
RBF kernel	Inverse multiquadric
Number of retained POD modes	64
RBF shape parameter	1.4
RBF smoothing parameter	1.0×10^{-5}

4.2. Temperature Field Reduction Using POD

POD is employed to reduce the dimensionality of the temperature fields under multiple operating conditions by mapping the high-dimensional temperature field onto a low-dimensional space represented by a limited number of modal coefficients. The dominant spatial modes are extracted from high-dimensional temperature field snapshots while the principal temperature distribution characteristics are retained [22].

Suppose that the training set contains N corrected complete temperature fields, all of which use the same spatial mesh and node numbering. The jth temperature field is expressed as

$$\boldsymbol{T}_j = \left[T_{1,j}, T_{2,j}, \ldots, T_{m,j}\right]^{\mathrm{T}} \tag{12}$$

where m is the number of spatial discrete points on the friction interface, and $T_{i,j}$ is the temperature at the ith spatial location under the jth operating condition.

The temperature fields under different operating conditions are arranged to form the snapshot matrix

$$\boldsymbol{X} = [\boldsymbol{T}_1, \boldsymbol{T}_2, \ldots, \boldsymbol{T}_N] \in \mathbb{R}^{m \times N}$$

where each column corresponds to a complete temperature field snapshot at a specific pressure, rotational speed, and sliding duration.

The mean temperature field of all samples is calculated as

$$\overline{\boldsymbol{T}} = \frac{1}{N}\sum_{j=1}^{N} \boldsymbol{T}_j \tag{13}$$

and the centered snapshot matrix is obtained by subtracting the mean temperature field from each snapshot:

$$\boldsymbol{X}_c = \left[\boldsymbol{T}_1 - \overline{\boldsymbol{T}}, \boldsymbol{T}_2 - \overline{\boldsymbol{T}}, \ldots, \boldsymbol{T}_N - \overline{\boldsymbol{T}}\right] \tag{14}$$

Singular value decomposition is performed on the centered snapshot matrix:

$$\boldsymbol{X}_c = \boldsymbol{U}\boldsymbol{\Sigma}\boldsymbol{V}^{\mathrm{T}} \tag{15}$$

where the columns of $\boldsymbol{U}$ are the POD spatial modes, $\boldsymbol{\Sigma}$ is the diagonal matrix of singular values, and $\boldsymbol{V}$ is the corresponding coefficient matrix. The magnitude of each singular value reflects the contribution of the corresponding POD mode to the variation in the original temperature field, and the dominant spatial characteristics are generally represented by the leading modes.

The cumulative energy contribution of the first r modes is calculated from the singular values as

$$E_r = \frac{\sum_{k=1}^{r} \sigma_k^2}{\sum_{k=1}^{q} \sigma_k^2} \tag{16}$$

where σ_k is the kth singular value and q is the total number of effective modes. When the cumulative energy contribution reaches the prescribed threshold, the first r modes are retained to form the reduced basis:

$$\Phi_r = [\varphi_1, \varphi_2, \ldots, \varphi_r]$$

where φ_k is the kth POD spatial mode.

The modal coefficients corresponding to the jth temperature field are obtained by projection:

$$\boldsymbol{a}_j = \Phi_r^{\mathrm{T}}\left(\boldsymbol{T}_j - \overline{\boldsymbol{T}}\right) \tag{17}$$

$$\boldsymbol{a}_j = \left[a_{1,j}, a_{2,j}, \ldots, a_{r,j}\right]^{\mathrm{T}} \tag{18}$$

The original temperature field is approximately reconstructed using the retained POD modes and the corresponding modal coefficients:

$$\hat{\boldsymbol{T}}_j = \overline{\boldsymbol{T}} + \Phi_r \boldsymbol{a}_j \tag{19}$$

where $\hat{\boldsymbol{T}}_j$ is the POD reconstructed temperature field.

Retaining dominant modes with high cumulative energy contributions reduces the data dimensionality while preserving the principal spatial characteristics of the temperature field. During model development, the POD basis is constructed from the temperature field snapshots of the 613 training samples after mean centering. Considering both the cumulative energy contribution and the predictive performance on the validation set, 64 POD modes are retained, accounting for more than 99.99% of the variance in the training snapshots. In addition, candidate ranks from 32 to 96 are evaluated. The results show that increasing the rank beyond 64 modes yields negligible further improvement in predictive performance. Therefore, 64 is selected as the truncation rank to balance prediction accuracy and model complexity.

4.3. Modal Coefficient Prediction Using RBF

After POD reduction, the complete temperature field under each operating condition is represented by the first r modal coefficients. The temperature-field prediction problem is therefore transformed into a nonlinear mapping from pressure, rotational speed, and sliding duration to the POD modal coefficients. RBF is used to establish this mapping, and the complete temperature field under an unseen operating condition is reconstructed using the predicted modal coefficients and the POD spatial modes.

For the jth temperature field sample, the operating condition vector is expressed as

$$\mathbf{x}_j = \left[p_j, n_j, t_j\right]^{\mathrm{T}} \tag{20}$$

where p_j, n_j, and t_j denote the pressure, rotational speed, and sliding duration of the jth sample, respectively. The corresponding POD modal coefficient vector is expressed as

$$\boldsymbol{a}_j = \left[a_{1,j}, a_{2,j}, \ldots, a_{r,j}\right]^{\mathrm{T}} \tag{21}$$

Before training the RBF model, each input feature and each retained POD modal coefficient is standardized separately by subtracting its training-set mean and dividing by its training-set population standard deviation. For any zero-variance variable, the scale factor is set to 1 to avoid division by zero. During parameter selection, the validation data are transformed using the training-derived statistics without recalculating the means or standard deviations. The predicted standardized POD coefficients are transformed back to their original scale using the corresponding means and standard deviations before temperature-field reconstruction.

The RBF model consists of an input layer, a radial basis function hidden layer, and an output layer. An inverse multiquadric radial basis function is adopted in this study. For an arbitrary input condition x, the response of the lth radial basis function is expressed as

$$\varphi(d_l) = \frac{1}{\sqrt{1 + (\varepsilon d_l)^2}} \tag{22}$$

where d_l denotes the Euclidean distance between the input vector x and the center c_l of the lth radial basis function, and ε is the RBF shape parameter. For an RBF hidden layer containing L radial basis functions, the predicted value of the kth POD modal coefficient is expressed as

$$\hat{a}_k(\boldsymbol{x}) = \sum_{l=1}^{L} w_{lk} \varphi_l(\boldsymbol{x}) + b_k \tag{23}$$

where w_{lk} is the connection weight between the lth radial basis function and the kth modal coefficient, and b_k is the bias term. After all r modal coefficients are predicted, the modal coefficient vector is obtained as

$$\hat{\boldsymbol{a}} = [\hat{a}_1, \hat{a}_2, \ldots, \hat{a}_r]^{\mathrm{T}} \tag{24}$$

which establishes the mapping from the operating-condition parameters to the low-dimensional temperature field representation:

$$[p, n, t] \rightarrow [\hat{a}_1, \hat{a}_2, \ldots, \hat{a}_r]$$

For the training samples, the radial basis function response matrix is constructed as

$$\boldsymbol{H} = \begin{bmatrix} \varphi_1(\boldsymbol{x}_1) & \cdots & \varphi_L(\boldsymbol{x}_1) \\ \varphi_1(\boldsymbol{x}_2) & \cdots & \varphi_L(\boldsymbol{x}_2) \\ \vdots & \ddots & \vdots \\ \varphi_1(\boldsymbol{x}_N) & \cdots & \varphi_L(\boldsymbol{x}_N) \end{bmatrix} \tag{25}$$

and the POD modal coefficients of all training samples are assembled into the output matrix

$$\boldsymbol{A} = \begin{bmatrix} a_{1,1} & a_{2,1} & \cdots & a_{r,1} \\ a_{1,2} & a_{2,2} & \cdots & a_{r,2} \\ \vdots & \vdots & \ddots & \vdots \\ a_{1,N} & a_{2,N} & \cdots & a_{r,N} \end{bmatrix} \tag{26}$$

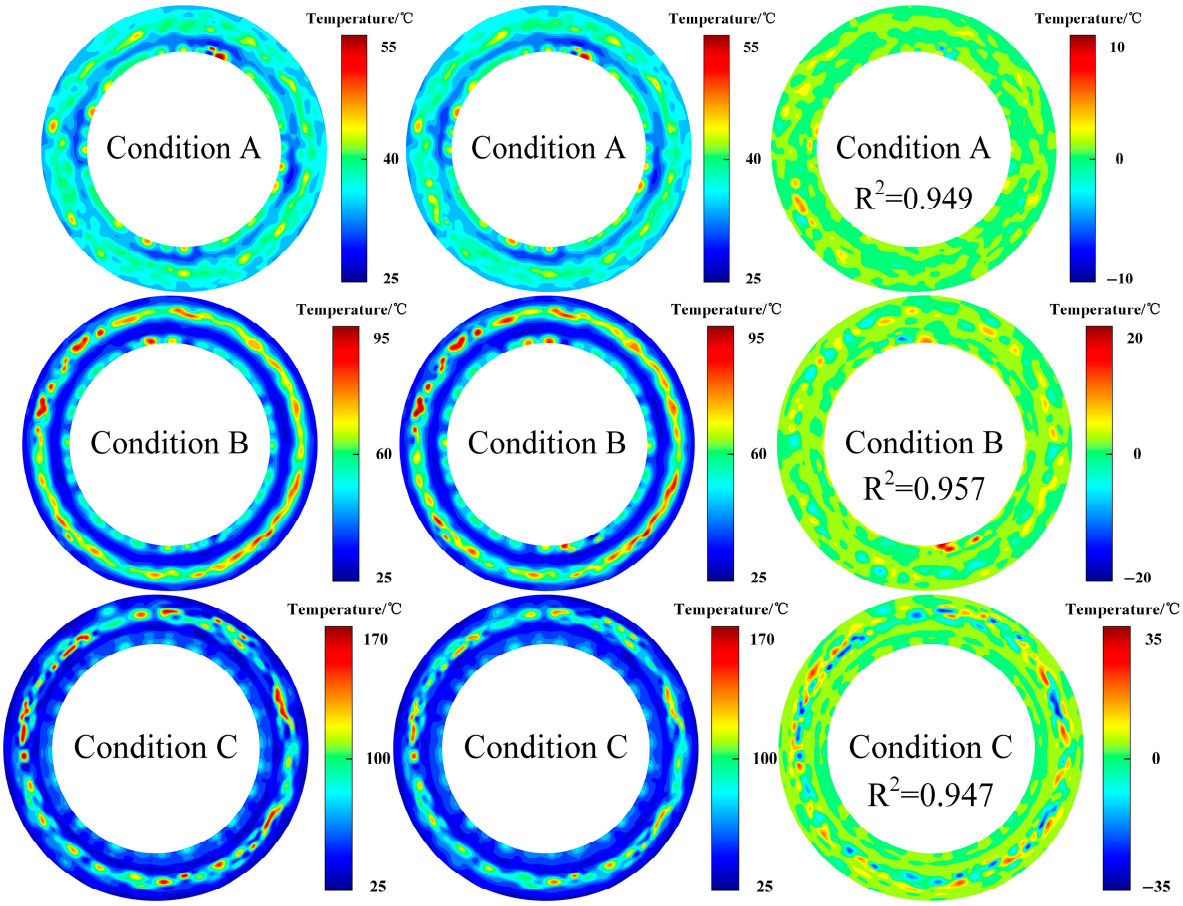
The RBF kernel function and its parameters are selected based on the validation performance. Eighteen configurations are evaluated by combining three kernel functions (inverse multiquadric, multiquadric, and Gaussian), three shape parameter values (0.6, 1.0, and 1.4), and two smoothing parameter values (10^{-5} and 10^{-3}). The inverse multiquadric kernel with a shape parameter of 1.4 and a smoothing parameter of 10^{-5} achieves the highest validation R^2 of 0.9621 and is therefore selected as the final configuration. This validation result is used for model selection, whereas the final predictive performance is assessed separately using the independent test set. Once the RBF model parameters are determined through training, the mapping between the operating-condition parameters and the POD modal coefficients is obtained. For an unseen operating condition, the corresponding POD modal coefficients are predicted by the trained RBF model, and the complete temperature field is reconstructed using the mean temperature field and the retained POD spatial modes.

5. Model Performance Validation

5.1. Validation of Prediction Results

To evaluate the predictive capability of the FEM-POD-RBF framework under operating conditions excluded from model development, three representative conditions, A, B, and C, are selected from the 130 independent test samples. These conditions were not included in the training or validation sets and were not used for preprocessing parameter estimation, POD basis construction, RBF model fitting, or hyperparameter selection. The experimentally corrected finite element temperature fields were used as reference fields and compared with the corresponding POD-RBF predictions. The prediction errors were also calculated. The reference temperature fields, predicted temperature fields, and error distributions for the three test conditions are presented in Figure 6. The predictions agree well with the reference fields in terms of the overall temperature level, the locations of high-temperature regions, and the radial and circumferential temperature distributions. The prediction errors are mainly concentrated in regions with large local temperature gradients, while no pronounced deviations are observed in the overall temperature distribution. These representative cases illustrate the reconstruction of the overall spatial temperature distribution. A quantitative

assessment of the high-temperature regions across all 130 test conditions is provided below to further characterize regional accuracy and localized errors.



(**a**) Reference temperature field (**b**) Predicted temperature field (**c**) Error field

Figure 6. Temperature-field prediction results.

For each test condition, the high-temperature region is defined as the spatial points with reference temperatures at or above the 90th percentile of that reference field. This definition identifies relatively hot locations within each temperature field. The corresponding predictions are extracted at the same spatial locations. All selected points from the 130 test conditions are pooled to calculate the regional R^2, MAE, and RMSE. The reference mean used for the regional R^2 is calculated over these selected points. The maximum absolute error is determined over the same high-temperature regions. The results are summarized in Table 5.

Table 5. Prediction performance of POD-RBF within the reference-defined high-temperature regions.

Metric	Value
Maximum absolute error	155.869 °C
R^2	0.9258
MAE	8.557 °C
RMSE	15.080 °C

To distinguish typical performance from worst-case behavior, the maximum absolute error within the high-temperature region is also calculated separately for each test condition. The median of these 130 condition-wise maximum errors is 19.762 °C. Maximum regional errors do not exceed 30 °C in 87 conditions, accounting for 66.92% of the test set, and do not

exceed 50 °C in 115 conditions, accounting for 88.46%. Errors exceeding 100 °C occur in four conditions. It should be noted that these large discrepancies are concentrated at a few isolated spatial locations rather than being distributed throughout the entire temperature field. Such errors may be associated with transient fluctuations in temperature measurements caused by mechanical vibrations during rotational sliding. These fluctuations may lead to abrupt changes at individual measurement points, and the resulting deviations may propagate to neighboring regions during spatial correction, ultimately causing relatively large prediction errors at a few isolated locations. All 130 conditions are retained in the evaluation. These results indicate that a single maximum absolute error does not adequately characterize model performance across different test conditions. The regional R^2, MAE, and RMSE reported in Table 5, together with the distribution of condition-wise maximum absolute errors, provide a more comprehensive assessment of prediction performance in high-temperature regions. Overall, POD-RBF captures temperature variations in these regions reasonably well, while large localized deviations are concentrated in a small number of conditions.

5.2. Model Performance Comparison

To further evaluate the temperature-field prediction performance of POD-RBF, POD combined with Gaussian Process Regression (POD-GPR), POD combined with Extreme Gradient Boosting (POD-XGBoost), Particle Swarm Optimization–Backpropagation Neural Network (PSO-BP), and Convolutional Neural Network (CNN) are selected as comparison models. The coefficient of determination (R^2), MAE, and RMSE are used as evaluation metrics. All models are trained and tested using the same temperature field dataset. Hyperparameters for all models were selected based on validation-set performance. POD-RBF, POD-GPR, and POD-XGBoost all retained 64 POD modes. POD-RBF and POD-GPR used grid search, whereas POD-XGBoost used TPE optimization and PSO-BP employed particle swarm optimization. CNN used a fixed network architecture, with the final training checkpoint selected based on validation-set performance. The prediction performance of each model is compared in Figure 7.

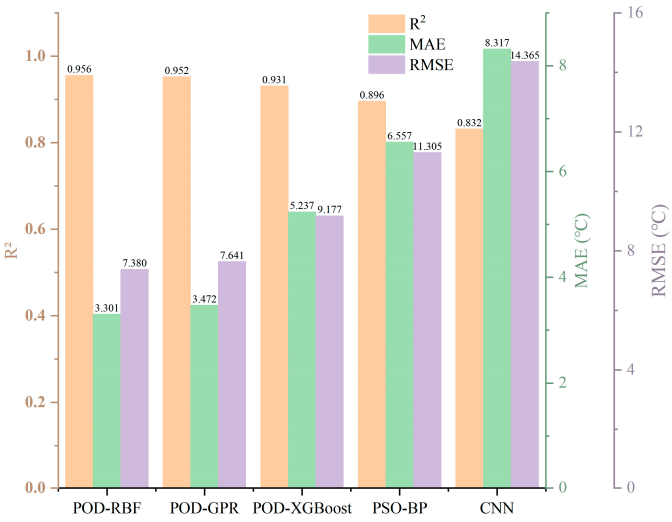


Figure 7. Performance comparison of different prediction models.

The models exhibit clear differences in prediction performance. POD-RBF achieves the highest R^2 of 0.956 and the lowest MAE and RMSE of 3.301 °C and 7.380 °C, respectively, indicating good agreement between the predicted and reference temperature fields. POD-GPR and POD-XGBoost generally outperform PSO-BP and CNN, demonstrating that POD

effectively extracts the dominant spatial characteristics of the temperature field and reduces the complexity of high-dimensional field prediction. Under the same POD reduction framework, POD-RBF produces lower prediction errors, indicating that RBF effectively captures the nonlinear relationship between the operating-condition parameters and the modal coefficients.

5.3. Sensitivity Analysis

The Morris global sensitivity analysis method is employed to evaluate the effects of model parameters and operating conditions on POD-RBF temperature-field prediction accuracy, using the coefficient of determination R^2 as the response. The input parameters and the model response are standardized to eliminate the effects of differences in parameter dimensions and ranges [23]. The mean absolute elementary effect of each parameter is defined as

$$\mu^* = \frac{1}{m}\sum_{l=1}^{m}\left|EE_i^{(l)}\right| \tag{27}$$

where μ^* is the mean absolute standardized elementary effect of the ith factor, m is the number of Morris sampling trajectories, and $EE_i{}^{(l)}$ is the standardized elementary effect of the ith factor along the lth trajectory. For each perturbation, the standardized elementary effect is calculated as

$$EE_i^{(l)} = \frac{Y(\boldsymbol{x}_{l,i} + \Delta_{l,i}\boldsymbol{e}_i) - Y(\boldsymbol{x}_{l,i})}{\Delta_{l,i} s_Y} \tag{28}$$

where Y denotes the model response, taken as the coefficient of determination R^2 in this study; $\boldsymbol{x}_{l,i}$ is the normalized parameter vector immediately before perturbing factor i along trajectory l; $\boldsymbol{e}_i$ is the unit vector in the direction of factor i; $\Delta_{l,i}$ is the signed normalized perturbation step; and s_Y is the sample standard deviation of the response across all evaluation points in the corresponding analysis.

The number of retained POD modes, the RBF shape parameter, and the smoothing parameter are selected for model-parameter sensitivity analysis. Contact pressure, rotational speed, and sliding duration are selected for operating-condition sensitivity analysis. The investigated ranges and sampling scales are summarized in Table 6.

Table 6. Parameter ranges used in the Morris sensitivity analyses.

Parameter	Range and Sampling Scale
Number of retained POD modes	32–96; linear
RBF shape parameter	0.40–1.60; linear
Smoothing parameter	10^{-6}–10^{-2}; logarithmic
Contact pressure	0.6–3 MPa; linear
Rotational speed	400–2000 rpm; linear
Sliding duration	0–1.5 s; linear

The factors are individually mapped to [0, 1] using the scales specified in Table 6. The smoothing parameter is represented on a base-10 logarithmic scale, and the mapped number of retained POD modes is rounded to the nearest multiple of 4. Each analysis uses six normalized levels, namely 0, 0.2, 0.4, 0.6, 0.8, and 1.0, with a normalized perturbation magnitude of 0.6. Each trajectory uses a randomly selected starting point, factor order, and perturbation directions. Only one factor is changed at each step, while the remaining factors are held constant and all factors remain within their specified ranges. Twenty-four trajectories are used for each analysis, each containing one starting point and three subsequent evaluation points, giving 96 evaluation points per analysis. For model-parameter sensitivity, the inverse multiquadric kernel is fixed, and each configuration is fitted using the same 613 training conditions and evaluated by pooled R^2 on the same 130 validation

conditions. POD and preprocessing are fitted exclusively to the training set. For operating-condition sensitivity, the trained model, POD basis, and preprocessing remain fixed, with condition-wise R^2 calculated between reference and predicted fields at matching nodes. These R^2 responses are used to calculate standardized elementary effects and subsequently μ^* according to Equation (27).

To facilitate comparison, the relative sensitivity weight of each factor is calculated by normalizing its μ^* within the corresponding analysis:

$$\omega_i = 100\% \times \mu_i^* / (\mu_1^* + \mu_2^* + \mu_3^*) \tag{29}$$

where ω_i is the relative sensitivity weight of the ith factor, and the denominator is the sum of μ^* for the three factors in the same analysis. Figure 8 presents the standardized sensitivity indices μ^* for the model parameters and operating conditions.

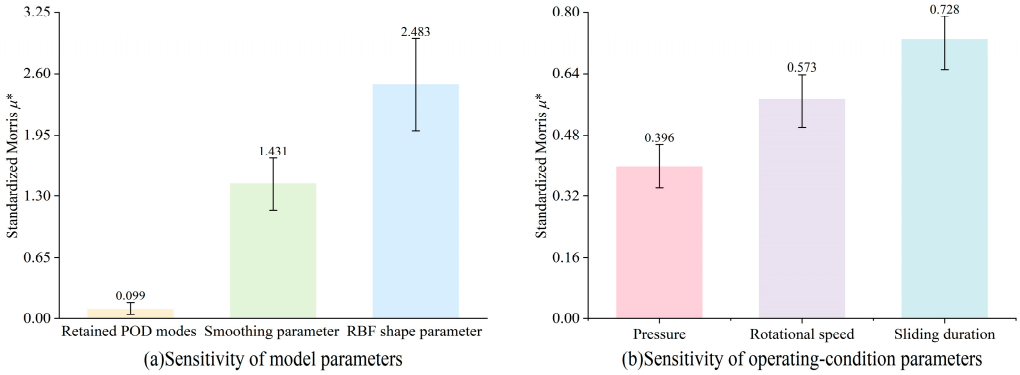


Figure 8. Morris sensitivity analysis of the POD-RBF model.

For the model parameters, the RBF shape parameter exhibits the highest sensitivity, with a μ^* of 2.483 and a relative sensitivity weight of 61.9%, indicating that it is the dominant parameter affecting the prediction accuracy of POD-RBF. The smoothing parameter has a sensitivity index of 1.431 and a relative weight of 35.6%, whereas the number of retained POD modes has a substantially lower sensitivity index of 0.099 and a relative weight of 2.5%. These results indicate that the RBF shape parameter has the greatest influence on prediction accuracy, while further increasing the number of retained POD modes provides only limited improvement.

The sensitivity results indicate that, within the investigated operating range, sliding duration has the greatest influence on prediction accuracy, followed by rotational speed and contact pressure. This ranking can be interpreted in terms of frictional heat generation and transient heat transfer. The instantaneous frictional heat flux is related to the contact pressure and the relative sliding velocity. When the other factors remain constant, increasing rotational speed increases the instantaneous frictional power. A longer sliding duration, in contrast, extends the period of heat input and allows heat to accumulate and diffuse into the friction components. Consequently, the temperature field evolves in both magnitude and spatial distribution. Changes in local temperature gradients and the development of high-temperature regions may increase the complexity of temperature-field reconstruction, helping to explain the high sensitivity of prediction accuracy to sliding duration. Contact pressure also affects frictional heat generation. However, the lower sensitivity of prediction accuracy to pressure in the present Morris analysis does not imply a weak thermal effect. The sensitivity indices are based on R^2 and quantify changes in prediction accuracy rather than changes in absolute temperature or total frictional heat. Within the investigated range, pressure produces a smaller variation in R^2 than sliding duration and rotational speed.

6. Effects of Operating Conditions

The experimental comparisons in Section 3 validate the accuracy of the finite element temperature responses at the measured locations under the tested conditions. Section 5 further validates the predictive accuracy of the POD-RBF model against the experimentally corrected finite element reference fields. Based on these validations, Sections 6.1 and 6.2 use predictions from the validated POD-RBF model and the corresponding derived temperature metrics to analyze the effects of pressure and rotational speed on the temperature field.

6.1. Effect of Pressure

The effect of pressure on the temperature field of the wet friction interface is investigated at a fixed rotational speed of 1500 r/min and a sliding duration of 0.5 s. Three pressure levels of 1.1, 1.6, and 2.1 MPa are selected, and the complete temperature fields are predicted using the POD-RBF model. The temperature field distributions under different pressures are presented in Figure 9. As the pressure increases, both the overall temperature level and the local high-temperature regions at the friction interface become more pronounced, while the radial and circumferential temperature gradients increase. This trend is consistent with the frictional heat generation mechanism, in which the frictional heat flux increases with contact pressure.

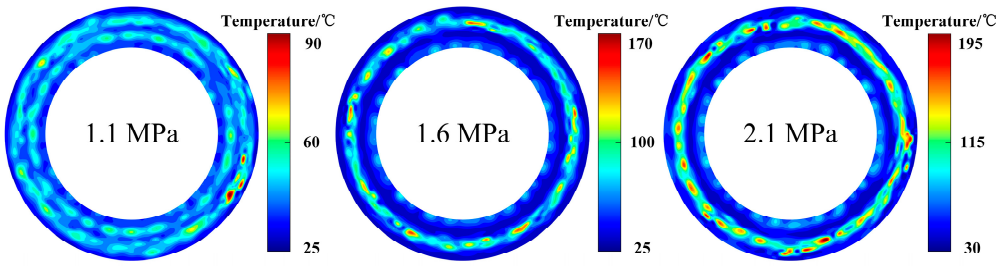


Figure 9. Temperature field distributions under different pressures.

To further quantify the effect of pressure on the temperature field, the average temperature rise ΔT_{mean}, the maximum radial temperature difference $\Delta T_{r,max}$, and the maximum circumferential temperature difference $\Delta T_{\theta,max}$ are extracted to characterize the overall temperature rise and the radial and circumferential temperature distribution characteristics. The corresponding results are presented in Figure 10.

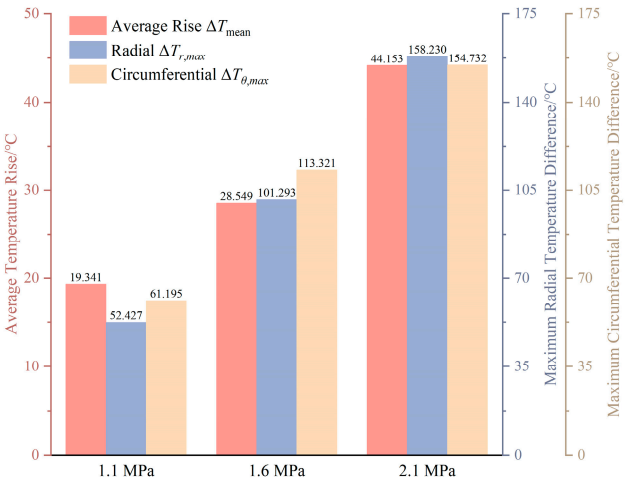


Figure 10. Temperature field characteristics under different pressures.

When the pressure increases from 1.1 to 2.1 MPa, the predicted mean temperature increases from 39.341 to 64.153 °C. The corresponding mean temperature rise increases from 19.341 to 44.153 °C, an increase of 128.3%. The maximum radial temperature difference increases from 52.427 to 158.230 °C, while the maximum circumferential temperature difference increases from 61.195 to 154.732 °C, corresponding to increases of 201.8% and 152.9%, respectively. The increases in both temperature differences are greater than that in the average temperature rise, with the radial temperature difference showing the largest increase. This indicates that increasing pressure has a stronger effect on spatial temperature nonuniformity than on the overall temperature rise. At higher pressure, the radial temperature difference exceeds the circumferential temperature difference, indicating a further increase in radial temperature nonuniformity.

6.2. Effect of Rotational Speed

The influence of rotational speed on the temperature field of the wet friction interface is examined at a fixed pressure of 1.6 MPa and a sliding duration of 0.5 s. Rotational speeds of 500, 1000, and 1500 r/min are selected, and the complete temperature fields are predicted using the POD-RBF model. The corresponding temperature distributions are presented in Figure 11. With increasing rotational speed, the overall temperature level of the friction interface rises markedly, the local high-temperature regions gradually expand, and the temperature difference between the high-temperature and low-temperature regions becomes larger, indicating an increase in spatial temperature nonuniformity.

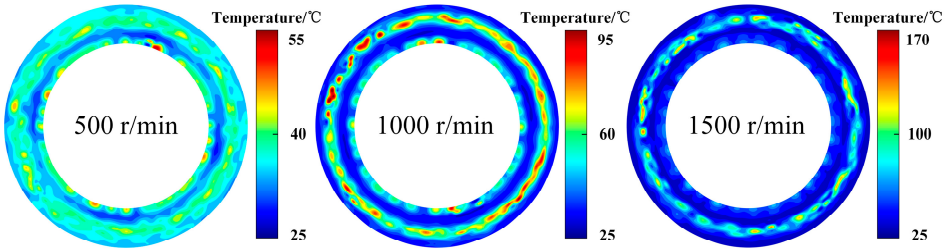


Figure 11. Temperature field distributions under different rotational speeds.

To quantitatively evaluate the effect of rotational speed on the temperature field characteristics, the average temperature rise, the maximum radial temperature difference, and the maximum circumferential temperature difference are further extracted, as presented in Figure 12.

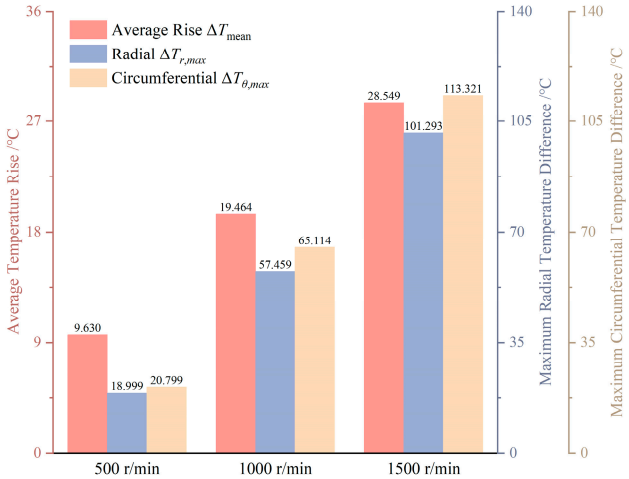


Figure 12. Temperature field characteristics under different rotational speeds.

When the rotational speed increases from 500 to 1500 r/min, the predicted mean temperature increases from 29.630 to 48.549 °C. The corresponding mean temperature rise increases from 9.630 to 28.549 °C, an increase of 196.5%. The maximum radial temperature difference increases from 18.999 to 101.293 °C, while the maximum circumferential temperature difference increases from 20.799 to 113.321 °C, corresponding to increases of 433.2% and 444.8%, respectively. The increases in both temperature differences are more than twice that of the average temperature rise, indicating that increasing rotational speed amplifies local temperature differences more strongly than the overall temperature rise. The circumferential temperature difference remains slightly higher than the radial temperature difference throughout the investigated range, indicating that circumferential temperature nonuniformity is more pronounced under these operating conditions.

7. Conclusions

An FEM-POD-RBF framework based on experimentally corrected finite element data is proposed for friction interface temperature-field prediction. Rapid prediction of the complete temperature field under different operating conditions is achieved through finite-element modeling, experimental temperature correction, POD reduction, and RBF mapping. The main conclusions are summarized as follows:

1. A finite-element model capable of reasonably characterizing the transient temperature rise of the wet friction interface is established. The finite element temperature field is corrected using the temperature residuals at the measurement points, allowing experimental temperature information to be incorporated while the complete spatial distribution characteristics are retained. The corrected temperature field therefore provides a complete dataset with experimental constraints for subsequent temperature-field prediction.
2. The POD-RBF model effectively achieves reduced-order representation and reconstruction of the high-dimensional temperature field. Good agreement is obtained between the predicted and reference temperature fields, with an R^2 of 0.956, an MAE of 3.301 °C, and an RMSE of 7.380 °C. Sensitivity analysis indicates that the RBF shape parameter has the greatest influence on model accuracy, followed by the smoothing parameter, while the number of retained POD modes has a relatively smaller influence. Within the investigated operating range, the prediction accuracy is most sensitive to sliding duration, followed by rotational speed, while pressure has a relatively smaller influence.
3. Increases in pressure and rotational speed intensify both the temperature rise and the spatial temperature nonuniformity at the friction interface. When the pressure increases from 1.1 to 2.1 MPa, the average temperature rise increases by 128.3%, while the radial and circumferential temperature differences increase by 201.8% and 152.9%, respectively. When the rotational speed increases from 500 to 1500 r/min, the average temperature rise increases by 196.5%, while both temperature differences increase by more than 430%. These results indicate that intensified operating conditions amplify local temperature differences more strongly than the average temperature rise.

The proposed approach has been evaluated within the investigated operating conditions and for the studied friction-pair configuration, while its applicability to a broader range of conditions requires further investigation. Future work will focus on expanding the experimental dataset and refining the model to further assess its applicability under diverse operating conditions.

Author Contributions: Conceptualization, J.W.; Methodology, X.J.; Validation, X.J. and N.R.; Formal analysis, J.W.; Investigation, N.R. and A.D.; Data curation, X.J., N.R. and A.D.; Writing – original draft,

X.J.; Writing – review & editing, J.W. and X.L.; Visualization, X.J. and A.D.; Supervision, X.L.; Project administration, X.L. All authors have read and agreed to the published version of the manuscript.

Funding: This research is supported by the National Natural Science Foundation of China (grant number 52175074). The APC is also supported by the National Natural Science Foundation of China (grant number 52175074).

Data Availability Statement: The data presented in this study are available on request from the corresponding author. (The data are not publicly available because the university and research group require prior authorization before research data can be shared externally.)

Conflicts of Interest: The authors declare no conflict of interest.

References

1. Zagrodzki, P. Numerical analysis of temperature fields and thermal stresses in the friction discs of a multidisc wet clutch. *Wear* **1985**, *101*, 255–271. [CrossRef]
2. Jen, T.C.; Nemecek, D.J. Thermal analysis of a wet-disk clutch subjected to a constant energy engagement. *Int. J. Heat Mass Transf.* **2008**, *51*, 1757–1769. [CrossRef]
3. Li, W.; Huang, J.; Fei, J.; Cao, L.; Yao, C. Simulation and application of temperature field of carbon fabric wet clutch during engagement based on finite element analysis. *Int. Commun. Heat Mass Transf.* **2016**, *71*, 180–187. [CrossRef]
4. Li, L.; Li, H.; Wang, L. Numerical analysis of dynamic characteristics of wet friction temperature fields. *Adv. Mech. Eng.* **2017**, *9*, 1–14. [CrossRef]
5. Lin, T.; Tan, Z.; He, Z.; Cao, H.; Lv, H.-S. Analysis of influencing factors on transient temperature field of wet clutch friction plate used in marine gearbox. *Ind. Lubr. Tribol.* **2018**, *70*, 241–249. [CrossRef]
6. Wu, J.; Ma, B.; Stanciulescu, I.; Li, H.; Wang, L. Experimental investigation of friction disc temperature field under cooling fluid. *Proc. Inst. Mech. Eng. Part C J. Mech. Eng. Sci.* **2021**, *235*, 3377–3388. [CrossRef]
7. Groetsch, D.; Voelkel, K.; Pflaum, H.; Stahl, K. Real-time temperature calculation and temperature prediction of wet multi-plate clutches. *Forsch. Ingenieurwesen* **2021**, *85*, 923–932. [CrossRef]
8. Jin, J.; Li, X.; Yang, S.; Sun, H.; Yi, H.; Hao, W. A temperature field model based on energy flow analysis of wet clutch sliding interface. *Tribol. Int.* **2024**, *199*, 109976. [CrossRef]
9. Rogkas, N.; Xypolias, G.; Drakopoulos, G.; Spitas, V. Coupled effect of lubricant fill volume on drag and friction torque of dip-lubricated wet clutches. *J. Tribol.* **2026**, *148*, 081117. [CrossRef]
10. Lei, J.; Liu, S. Temperature field reconstruction from the partial measurement data using the gappy proper orthogonal decomposition. *IET Sci. Meas. Technol.* **2013**, *7*, 171–179. [CrossRef]
11. Jiang, G.; Kang, M.; Cai, Z.; Wang, H.; Liu, Y.; Wang, W. Online reconstruction of 3D temperature field fused with POD-based reduced order approach and sparse sensor data. *Int. J. Therm. Sci.* **2022**, *175*, 107489. [CrossRef]
12. Wang, X.; Cao, Z.; Liu, Y.; Wang, F. Temperature reconstruction in data centers using gappy POD combined with genetic algorithm and optimization of sensor layout. *Energy Build.* **2025**, *326*, 115078. [CrossRef]
13. Peng, X.; Chen, Z.; Zhang, A.; Chen, X.; Zhang, Y. Digital twin temperature field prediction of laser powder bed fusion through proper orthogonal decomposition with radial basis function. *Mater. Today Commun.* **2024**, *38*, 107883. [CrossRef]
14. Liu, Y.; Zhao, Q.; Liu, G.; Zou, Y.; Zhang, S.; Wang, K.; Zhao, X. A real-time solution method for three-dimensional steady temperature field of transformer windings based on mechanism-embedded cascade network. *Case Stud. Therm. Eng.* **2024**, *58*, 104444. [CrossRef]
15. Zhao, W.; Zhang, B. Temporal extrapolation generalization of proper orthogonal decomposition (POD) and radial basis function (RBF) surrogates for transient thermal fields in multi-heat-source electronic devices. *Micromachines* **2025**, *16*, 1267. [CrossRef] [PubMed]
16. Rogkas, N.; Patsouras, D.; Lazaridis, C.; Zalimidis, P.; Rakopoulos, D.; Spitas, V. Optimal groove design for viscous drag reduction in wet clutch lubrication to enhance energy-efficiency in power transmissions. *Energy* **2026**, *348*, 140376. [CrossRef]
17. Cai, Y.; Wang, Z.; Wang, H.; Hu, M. Temperature field and its influencing factors of friction pair of wet clutch of hybrid electric vehicle. *J. Chongqing Univ.* **2024**, *47*, 93–103. [CrossRef]
18. Shin, S.; Choi, S.B. Control-oriented modeling of wet clutch friction considering thermal dynamics. *Mechatronics* **2024**, *99*, 103146. [CrossRef]
19. Liu, Y.; Wei, C.; Wu, W.; Cheng, L.; Wang, X.; Zhao, J. Simulated and measured characteristics for churning oil flow with a coating surface over a wide range of temperatures. *Friction* **2025**, *14*, 9441192. [CrossRef]
20. Wei, C.; Wu, W.; Zhao, N.; Li, T.; Liu, Y.; Nelias, D.; Li, X. Investigation of lubricant flow in a planetary bearing cavity under stationary carrier condition. *Tribol. Int.* **2026**, *215*, 111458. [CrossRef]

21. Chen, M.; Zhang, B.; Feng, Y.; Wang, L.; Wang, H. Numerical and experimental studies of the attenuation characteristics of friction torque in a wet multidisc clutch. *Appl. Sci.* **2021**, *11*, 814. [CrossRef]
22. Matulis, J.; Bindra, H. Thermal field reconstruction and compressive sensing using proper orthogonal decomposition. *Front. Energy Res.* **2024**, *12*, 1336540. [CrossRef]
23. Shi, W.; Zhou, Q.; Zhou, Y. An efficient elementary effect-based method for sensitivity analysis in identifying main and two-factor interaction effects. *Reliab. Eng. Syst. Saf.* **2023**, *237*, 109365. [CrossRef]

Disclaimer/Publisher's Note: The statements, opinions and data contained in all publications are solely those of the individual author(s) and contributor(s) and not of MDPI and/or the editor(s). MDPI and/or the editor(s) disclaim responsibility for any injury to people or property resulting from any ideas, methods, instructions or products referred to in the content.